Numerical models of caldera deformation: Effects of multiphase and multicomponent hydrothermal fluid flow

M. Hutnak,[1] S. Hurwitz,[1] S. E. Ingebritsen,[1] and P. A. Hsieh[1]

[1]   Ground surface displacement (GSD) in large calderas is often interpreted as resulting from magma intrusion at depth. Recent advances in geodetic measurements of GSD, notably interferometric synthetic aperture radar, reveal complex and multifaceted deformation patterns that often require complex source models to explain the observed GSD. Although hydrothermal fluids have been discussed as a possible deformation agent, very few quantitative studies addressing the effects of multiphase flow on crustal mechanics have been attempted. Recent increases in the power and availability of computing resources allow robust quantitative assessment of the complex time-variant thermal interplay between aqueous fluid flow and crustal deformation. We carry out numerical simulations of multiphase (liquid-gas), multicomponent (H_2O-CO_2) hydrothermal fluid flow and poroelastic deformation using a range of realistic physical parameters and processes. Hydrothermal fluid injection, circulation, and gas formation can generate complex, temporally and spatially varying patterns of GSD, with deformation rates, magnitudes, and geometries (including subsidence) similar to those observed in several large calderas. The potential for both rapid and gradual deformation resulting from magma-derived fluids suggests that hydrothermal fluid circulation may help explain deformation episodes at calderas that have not culminated in magmatic eruption.

1.   Introduction

[2]   Measured ground surface displacement (GSD) rates in calderas span several orders of magnitude, from mm a^{-1} (detection limit) to m a^{-1}, over periods of observation that range from subannual to millennial [e.g., *Dvorak and Dzurisin*, 1997; *Dzurisin*, 2003, 2007; *Poland et al.*, 2006]. Modern geodetic techniques such as interferometric synthetic aperture radar (InSAR) and GPS provide unprecedented insight into the temporal and spatial evolution of GSD, and reveal that deformation patterns can be highly variable both in space and in time [e.g., *Battaglia and Segall*, 2004; *Chang et al.*, 2007; *Kwoun et al.*, 2006; *Wicks et al.*, 2006]. Deformation patterns have traditionally been interpreted to result from magmatic intrusion into the shallow crust, with intrusion source depth, volume, and geometry often calculated using analytical elastic half-space models [e.g., *Fialko et al.*, 2001; *Mogi*, 1958] that are sensitive to simplified assumptions [e.g., *Manconi et al.*, 2007; *Masterlark*, 2007]. In fact, most reported GSD episodes have not culminated in magma eruption, and eruptions can occur without significant observed GSD [e.g., *Pritchard and Simons*, 2002]. Magma intrusion acts as a volume and pressure source, but an intrusion into the deep crust can also provide heat and volatiles required to drive hydrothermal circulation in the overlying permeable crust. At longer time scales, magma crystallization is a major source for heat and volatiles (mainly H_2O and CO_2) that enter the overlying hydrothermal system. Circulation of hydrothermal fluids promotes rock thermal expansion and contraction, as do pressure changes due to fluid injection and gas formation.

[3]   An increasing number of observations indicate a causal link between transient groundwater and/or gas pressures and GSD in volcanoes [e.g., *Battaglia et al.*, 2006; *Chiodini et al.*, 2003; *Dzurisin et al.*, 1990; *Gottsmann et al.*, 2007; *Watson et al.*, 2000]. Further, many caldera-hosted hydrothermal systems likely include vapor-dominated, two-phase regions with large CO_2 fractions in the gas phase [*Chiodini et al.*, 2001, 2003; *Lowenstern and Hurwitz*, 2008; *Werner and Brantley*, 2003]. This suggests that caldera deformation can be induced by multiphase, compressible fluids in a permeable medium.

[4]   Recent numerical modeling studies have indeed demonstrated that rates of GSD measured by geodetic techniques could theoretically be induced by poroelastic transients in the shallow hydrothermal system [*Hurwitz et al.*, 2007; *Todesco et al.*, 2004]. *Todesco et al.* [2004] carried out simulations using a multiphase, multicomponent (H_2O-CO_2) fluid to describe the recent evolution of a shallow (1.5 km deep) hydrothermal system in the Campi Flegrei Caldera (Italy), and *Hurwitz et al.* [2007] carried out simulations using a single-component (H_2O) fluid with the

---

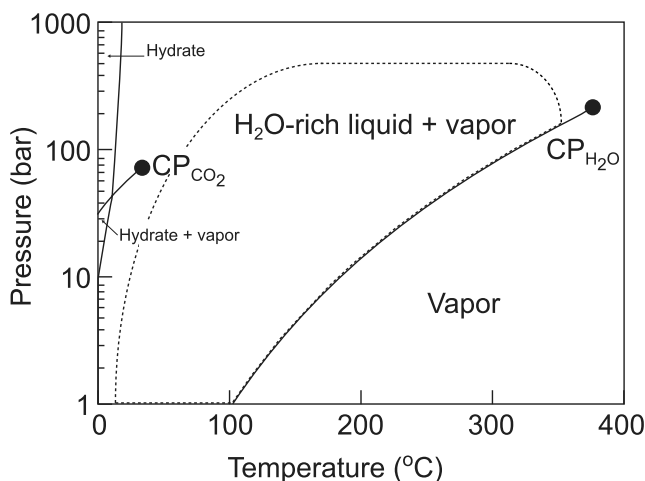[1]U.S. Geological Survey, Menlo Park, California, USA.

Figure 1. Pressure-temperature projection of the H_2O and CO_2 phase diagrams, showing liquid-vapor coexistence curves and critical points (CP) for pure H_2O and pure CO_2. Coexistence curves for H_2O–CO_2 mixtures will lie between these two end-members. The dashed outline encompasses P-T space considered in this study.

goal of determining the range of plausible conditions under which poroelastically induced GSD might occur.

[5] In this study we build upon the work of *Hurwitz et al.* [2007] and examine the effects of a multiphase (liquid–gas), multicomponent (H_2O–CO_2) hydrothermal fluid on caldera deformation. In particular, we (1) examine the temporal and spatial evolution of GSD (rates, magnitudes, geometries) by comparing single-component and multicomponent simulation results using a range of hydrologically realistic properties and processes and (2) explain the complex thermal interplay between fluid flow, GSD, and gas fluxes at the ground surface.

2. Magmatic Hydrothermal Fluids

[6] The flux and composition of magmatic fluids entering caldera-hosted hydrothermal systems depend in part on the depth, composition, degree of evolution, and dimensions of the underlying magma body [*Fournier*, 1999; *Giggenbach*, 1984, 1988]. After H_2O, CO_2 is the most abundant volatile component dissolved in magmas. As magmas crystallize, or intrusions ascend in the crust, volatile solubility in the magma decreases. Because CO_2 solubility is lower than that for H_2O at equivalent temperatures and pressures, the relative proportion of CO_2 in a separate gas phase increases with depth [*Lowenstern*, 2001].

[7] Measured CO_2 surface fluxes in large calderas range from 250 t d^{-1} in Long Valley [*Gerlach et al.*, 1999] to 45,000 t d^{-1} in Yellowstone [*Werner and Brantley*, 2003]. Magmatic H_2O fluxes are poorly constrained; some evidence from melt inclusions trapped in crystals ejected in large eruptions suggest H_2O:CO_2 mass ratios ranging from 5:1 in Mono Craters, California [*Newman et al.*, 1988], to 300:1 in the Bishop Tuff of Long Valley, California [*Anderson et al.*, 1989]. However, these ratios are probably upper limits, because much of the CO_2 was likely degassed from the magma at depths greater than the entrapment depths of the melt inclusions.

[8] As magmatic volatiles enter the hydrothermal system, the phase distribution depends on thermodynamic conditions and fluid composition. The critical point for pure H_2O is 374.2°C and 22.05 MPa and is much higher than that for pure CO_2 (31.1°C and 7.38 MPa) (Figure 1). In mixtures of H_2O and CO_2, single and multiple phases of gas-rich and liquid-rich fluids can exist in equilibrium over a range of intermediate pressure-temperature conditions [*Duan and Zhang*, 2006; *Kaszuba et al.*, 2006].

3. Conceptual Model

[9] We base our numerical model on a widely cited conceptual model of volcano-hydrothermal systems [*Fournier*, 1999]. Aqueous fluids derived from crystallizing or convecting magma, or from episodic dike intrusion into crystallizing magma, are sourced into the base of the overlying hydrothermal system. Injection of high-temperature fluids can induce fluid overpressures, causing the porous rock to inflate, with the degree of inflation controlled in part by rock rigidity. Rock expansion/contraction induced by temperature and fluid pressure cause deformation (both uplift and subsidence) as hydrothermal fluids circulate in the shallow crust.

[10] For multiphase systems, the reduction in flow of one phase due to the interfering presence of the other phase can be described using relative permeabilities (k_r). These are empirically based functions of volumetric saturation of liquid (k_{rl}) and gas (k_{rg}) phases, with values of k_r varying between 0 and 1. Production data from several geothermal fields seem to indicate that interference between the phases is insignificant ($k_{rl} + k_{rg} = 1$ [e.g., *Horne and Ramey*, 1978; *Sorey et al.*, 1980]), whereas some laboratory data for unconsolidated porous media suggest $k_{rl} + k_{rg} \ll 1$ over a large saturation range [e.g., *Corey*, 1957; *Li and Horne*, 2007; *Piquemal*, 1994]. Because relative permeabilities are sensitive to pore and fracture geometry, the appropriate functional relationship will likely vary within the system of interest. Two of the most widely used relationships are linear and Corey-type curves, and with a few exceptions, the models in the present study incorporate Corey-type relative permeability functions.

4. Numerical Model

[11] We couple two numerical codes in order to simulate the poroelastic effects of magmatic fluid injection into the shallow hydrothermal system. TOUGH2 [*Pruess*, 2005] is a three-dimensional integrated finite difference simulator for nonisothermal, multicomponent and multiphase fluid flow in porous or fractured media. BIOT2 [*Hsieh*, 1996] simulates axisymmetric or plane strain deformation in an elastic porous medium. Details about the coupling of the two codes are given by *Hurwitz et al.* [2007]. We use the EOS2 module of TOUGH2, which incorporates CO_2-H_2O equations of state in the temperature and pressure range 0–350°C and 0–100 MPa, respectively [*Spycher et al.*, 2003].

[12] Natural calderas are quasi-circular in map view, and we take advantage of this geometry by generating a radially symmetric model domain 5 km thick with a radius of 50 km or greater (Figure 2). The model grid and results can be visualized on a rectangular cross section, with the left edge
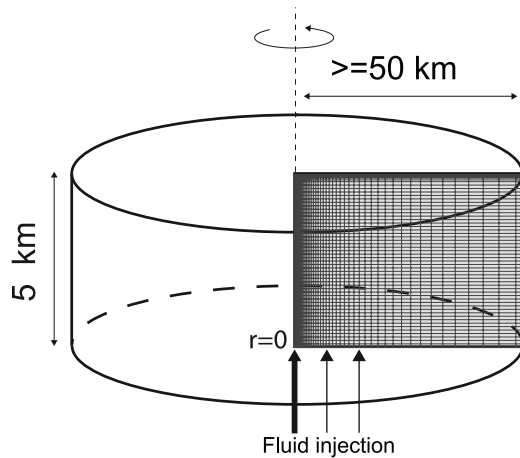
Figure 2. Radially symmetric computational model domain, with boundary conditions described in the text. Fluids are injected into the base of the model domain at r = 0 for point source simulations (thick arrow) and injected over a radial distance of 9.5 km for distributed source simulations (thick and thin arrows).

of the cross section coinciding with the central axis of the caldera. Horizontal grid spacing is 25 m at the center of the domain and increases logarithmically outward to 5 km at the caldera margin. Vertical grid spacing is 0.01 m at the top of the model and increases stepwise downward to a depth of 150 m, with 100 m thick layers throughout the remainder of the domain.

[13] Boundary conditions imposed on TOUGH2 at the left (center of the caldera) and right (outer edge of the caldera) sides of the mesh are insulating and impermeable. The upper (ground surface) boundary is maintained at a constant temperature of 10°C and a pressure of 0.1 MPa to represent water table conditions. The lower boundary, representing the base of the hydrothermal system, has constant heat flux and is impermeable except at locations where fluids are being injected. Boundary conditions for BIOT2 include no displacement on the right and bottom boundaries, vertical displacement only on the left boundary, and a traction-free surface on the upper boundary. Initial conditions consist of a hydrostatic pressure distribution throughout the model domain and a linear temperature distribution based on the fixed-temperature upper boundary and constant heat flux lower boundary.

[14] Rock properties are homogeneous and isotropic, and fluids are sourced at constant rates into the base of the model domain. Fluids are injected either as a "point source" in the majority of our simulations (from a single grid block in the center of the model domain, representing an area of $\sim$500 m^2), or as a "distributed source" (injection from 45 grid blocks over a radial distance of 9.5 km, representing an area of $\sim$300 km^2) (Figure 2). We assume that the water table coincides with the ground surface and that the topography is flat (in contrast to stratovolcanoes where topography influences hydrodynamics [Hurwitz et al., 2003]). Furthermore, we invoke a one-way coupling; that is we do not consider the effect of stress changes on permeability, porosity, or fluid flow. The effect of simulated deformation on permeability, for example, is expected to be much smaller than the permeability range tested here [Hurwitz et al., 2007].

[15] The range of plausible values for most simulation parameters is large. Parameters that display a high degree of variability in nature include rock permeability, porosity, and elastic moduli, as well as the magnitude of fluid sourcing and basal heat flux. A previously published parameter sensitivity analysis showed that model results are particularly sensitive to fluid injection rates, permeability, fluid source depth, and the shear modulus [Hurwitz et al., 2007].

[16] For the present study, we employ a range of hydrologically plausible parameters applicable to large calderas with a hydrothermally active zone 5 km thick (Table 1). The thickness of this zone represents the depth to the brittle-ductile transition, which ranges between four and eight kilometers in several analogous natural systems [Hill, 1992; Sherburn et al., 2003]. Permeabilities considered are 10^{-16} to 10^{-15} m^2, consistent with continental [Manning and Ingebritsen, 1999] and geothermal field [Bjornsson and Bodvarsson, 1990] values for the depth range considered. Fluid injection rates are varied between 2 and 21 kt d^{-1} with a 20:1 mass ratio of water to carbon dioxide, consistent with the range of CO$_2$ fluxes estimated in several comparable natural systems [Chiodini et al., 2001; Gerlach et al., 1999; Goff and Janik, 2002; Seward and Kerrick, 1996]. The value of thermal conductivity (2.8 W m^{-1} °C^{-1}) is an average for the continental crust, and basal heat flux (100 mW m^{-2}) is consistent with available data for Quaternary calderas [Bibby et al., 1995; Lachenbruch et al., 1976; Wohletz et al., 1999]. Typical values for the thermal expansion coefficient for saturated rock at high temperature and pressure range from 5×10^{-6} °C^{-1} to 1.5×10^{-5} °C^{-1} [Bauer and Handin, 1983; Heard and Page, 1982; Wong and Brace, 1979], and we use a value of 1×10^{-5} °C^{-1} in all simulations. Crustal deformation scales inversely with shear (rigidity) modulus, and laboratory experiments at high pressures and temperatures indicate that the intrinsic shear modulus of crystalline rocks varies from 0.2 to 50 GPa depending on rock type, temperature, pressure, and porosity [Heard and Page, 1982]. Although large-scale crustal values of 30 GPa [Turcotte and Schubert, 2002] are commonly invoked in elastic deformation models, several studies have suggested that the rigidity of warm volcanic rocks should be as low as 0.3 GPa [e.g., Davis, 1986]. We set the shear modulus at 1 GPa in the examples discussed here. We assume that the solid grains of the host rock are much less compressible than the bulk medium and therefore

Table 1. Model Parameters

Parameter/Process	Range Tested
H$_2$O injection rate	2$-$21 kt d^{-1}
CO$_2$ injection rate	0.1$-$1 kt d^{-1}
Injection area	500 m^2, 300 km^2
Permeability	10^{-15} m^2, 10^{-16} m^2
Fluid source depth	5 km
Shear modulus	1 GPa
Porosity	10%
Basal heat flux	100 mW m^{-2}
Thermal conductivity	2.8 W m^{-1} K^{-1}
Rock grain density	2700 kg m^{-3}
Rock grain specific heat	1000 J kg^{-1} °C^{-1}
Source temperature	350°C
Thermal expansion coefficient	1×10^{-5} °C^{-1}
Biot-Willis coefficient	1
Poisson's ratio	0.25
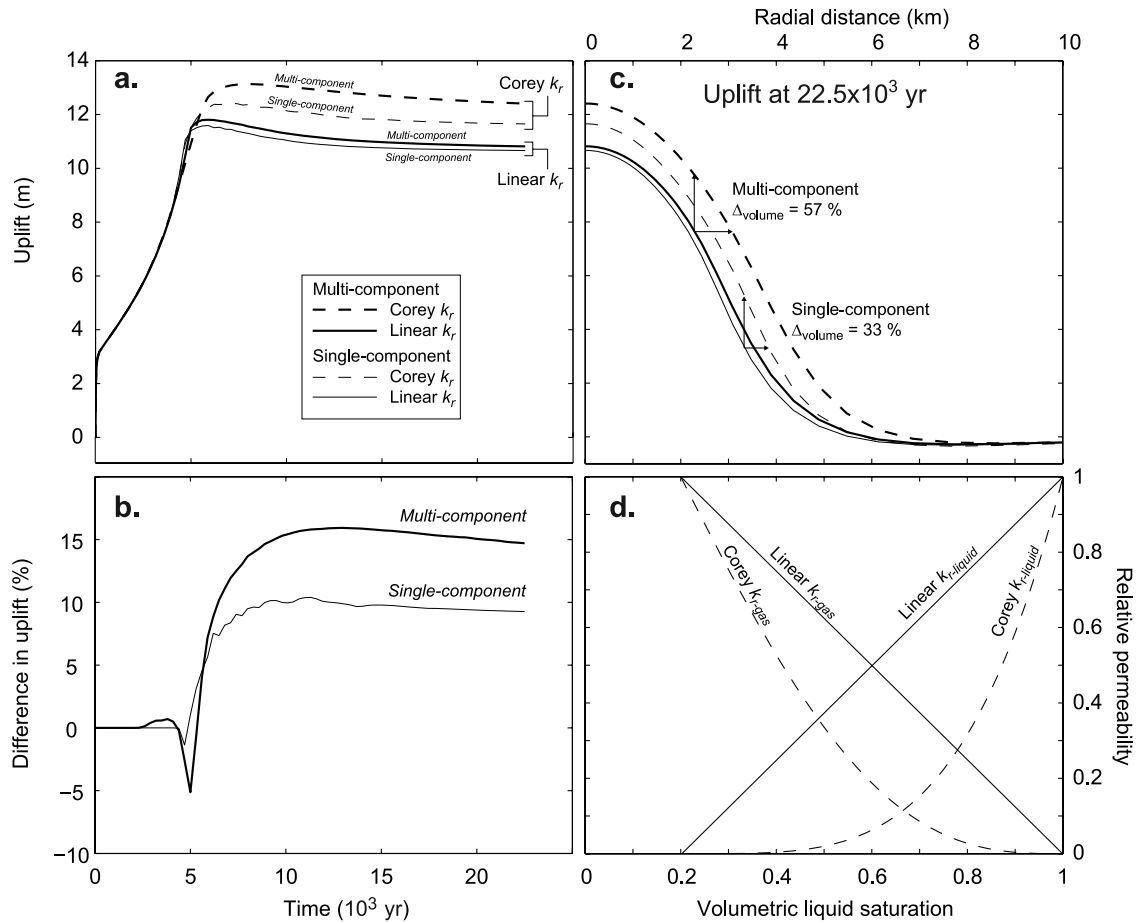
Figure 3. Deformation resulting from constant rate fluid injection of 20 kt d^{-1} H$_2$O and 1 kt d^{-1} CO$_2$ into host rock having a permeability of 10^{-15} m^2. Thick lines show model results for a multicomponent (H$_2$O–CO$_2$) system; thin lines show results for a pure water system. Dashed lines show results determined using Corey-type relative permeability (k_r) functions; solid lines show results for linear k_r functions. (a) Cumulative deformation at the center of the caldera for the four configurations tested. (b) Percentage difference in uplift between Corey-type and linear k_r for single-component and multicomponent simulations. (c) Vertical and radial extent of deformation for the four configurations tested, showing a significant increase in volume when gas formation impedes vertical fluid flow. (d) Relationship between Corey-type and linear relative permeability functions.

set the Biot-Willis coefficient to 1. Fluids are injected into the base of the hydrothermal zone at a temperature of 350°C, consistent with thermal conditions in the brittle crust.

[17] In order to assess the effects of a multicomponent (H$_2$O–CO$_2$) hydrothermal fluid on caldera deformation, we perform a series of "baseline" simulations in which an equivalent amount of single-component (H$_2$O) fluid is sourced into the base of the model domain. For example, results from a multicomponent simulation incorporating 20 kt d^{-1} of H$_2$O and 1 kt d^{-1} of CO$_2$ are compared with those from a simulation containing 21 kt d^{-1} of pure H$_2$O.

5. Simulation Results

5.1. Point Source Simulations

[18] In models of multiphase systems, the functional relationship used to describe the reduction in flow of one phase due to the presence of the other phase (relative permeability) can have significant effects. The most widely used relationships for relative permeability are Corey-type

curves and we employ these in nearly all simulations. Figure 3 compares simulated GSD for Corey and linear relative permeability relations for a simulation in which 20 kt d^{-1} of H$_2$O and 1 kt d^{-1} of CO$_2$ are sourced into a host rock having a permeability of 10^{-15} m^2. GSD magnitude and radial extent are larger in simulations employing Corey-type relationships, with uplift in the center of the domain increasing by 9–15% and volume increasing by 33–57% relative to simulations employing the linear relationships. Sensitivity to other key parameters was explored by *Hurwitz et al.* [2007].

[19] The effects of point source hydrothermal fluid injection rates and subsequent circulation on GSD for permeabilities of 10^{-15} and 10^{-16} m^2 are shown in Figures 4 and 5, respectively. Animations 1–6[1] show the evolution of the temperature and gas saturation fields. Rocks hosting the hydrothermal system deform poroelastically due to increased
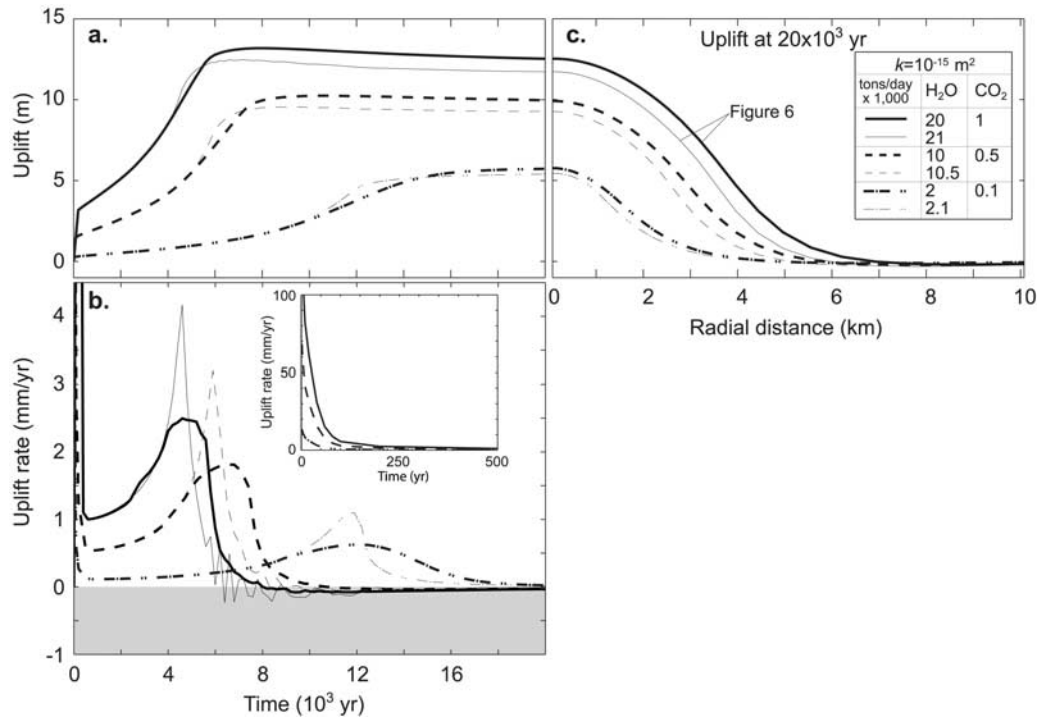
---

[1]Animations are available in the HTML.

Figure 4. Deformation resulting from constant fluid injection into host rock having a permeability of 10^{-15} m^2. Thick lines show model results for multicomponent (H_2O-CO_2) system; thin lines show results for a pure water system. Multicomponent simulations lead to greater vertical and radial extents of deformation over time. (a) Cumulative deformation at the center of the domain as a function of time for the six source configurations tested. (b) Uplift rates at the center of the domain as a function of time; gray shading identifies region of negative uplift rates (subsidence), and inset shows high initial rates. (c) Vertical and radial extent of deformation after 20,000 years. Vertical cross sections showing gas saturation for the highest fluid injection rates are shown in Figure 6. Animations 1–3 show system evolution.

fluid pressure during fluid injection and gas formation, and thermoelastically due to rock thermal expansion as buoyant, high-enthalpy fluids migrate toward the ground surface. Immediately following the onset of fluid injection through the base of the model domain, an overpressured zone with elevated temperatures develops near the injection point, causing local deformation. This deformation is manifested at the ground surface as rapid uplift in the center of the domain. The deformed volume expands with time, and gradual uplift in the center continues as hot fluids migrate vertically and warm the host rock. At later times, pressure increases within the shallow subsurface (0–1 km) due to formation of a gas phase increase both the vertical and radial extent of deformation (Figure 6).

[20] GSD rate, magnitude, and radial extent are strongly influenced by crustal permeability. When permeability is 10^{-15} m^2, uplift of ~12 m is attained in the center of the caldera for the highest injection rate tested after 7000 simulation years (Figure 4a, thick solid line, Animation 1), after which there is gradual subsidence. Lower sourcing rates lead to less uplift (Figure 4a, thick dashed lines, Animations 2 and 3), and the time required to attain maximum uplift scales inversely with injection rate. Uplift rates are highest at the onset of fluid sourcing (Figure 4b, inset), with maximum values between 10 and 100 mm a^{-1}. Uplift rates in the center of the domain decrease to <2 mm a^{-1} after several

tens to hundreds of simulated years (Figure 4b, thick lines), before gradually increasing again as pockets of gas develop in the shallow subsurface. Once deformation has accommodated the large volume change associated with shallow gas formation, uplift rates decrease, and even become negative (indicating subsidence) at later times for the two highest injection rates shown. The radial extent of deformation scales with injection rate, from ~4–7 km for the rates tested (Figure 4c, thick lines).

[21] When crustal permeability is an order of magnitude lower (10^{-16} m^2), pore pressures at depth are higher, and both the magnitude of uplift and radial extent of deformation are enhanced (Figures 5a and 5c, thick lines. Animations 4, 5, and 6), achieving maximum values of 32 m and 15 km, respectively. Uplift rates in the caldera center are highest during the first tens to hundreds of simulated years (Figure 5b, inset), with values between 20 and 160 mm a^{-1} for the injection rates tested. Rates then drop dramatically to <0.5 mm a^{-1} (Figure 5b, thick lines), and become negative (indicating subsidence) at later times for the two highest injection rates shown.

[22] Formation of gas (steam and CO_2) has a significant impact on GSD rate, magnitude, and geometry for a given permeability (compare thick and thin lines in Figures 4 and 5). Inclusion of CO_2 tends to generate greater vertical and radial extents of deformation because the vertical extent of
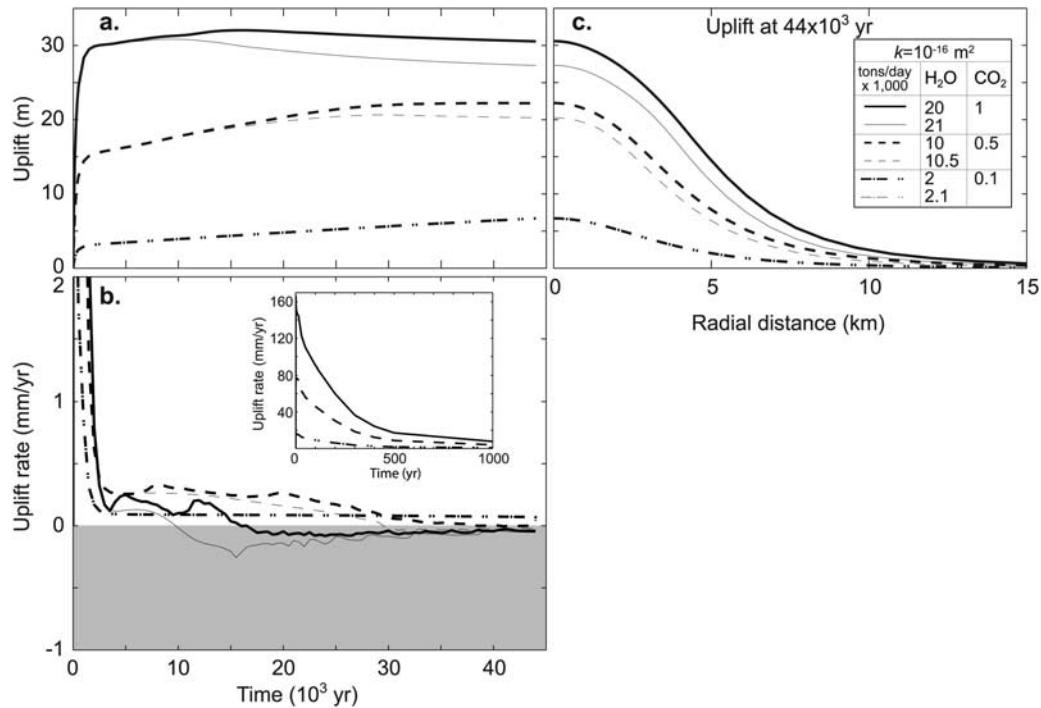
Figure 5. Deformation resulting from constant fluid injection into host rock having a permeability of 10^{-16} m^2. Thick lines show model results for multicomponent (H_2O-CO_2) system; thin lines show results for a pure water system. Curves are visually indistinguishable for the lowest injection rate shown. Multicomponent simulations lead to greater vertical and radial extents of deformation over time. (a) Cumulative deformation at the center of the domain as a function of time for the six source configurations tested. (b) Uplift rates at the center of the caldera as a function of time; gray shading identifies region of negative uplift rates (subsidence), and inset shows high initial rates. (c) Vertical and radial extent of deformation after 44,000 years. Animations 4–6 show system evolution.

boiling is enhanced, causing a larger fraction of the host rock to experience large volume (i.e., pressure) changes and reductions in relative permeability associated with gas formation (Figure 3). Figure 6 displays the extent of gas saturation during equivalent time slices for a single-component and multicomponent simulation where permeability is 10^{-15} m^2 (Figure 4c). In the pure H_2O simulation, water vapor saturations exceed 10% over a depth range of 25 to 1250 m and
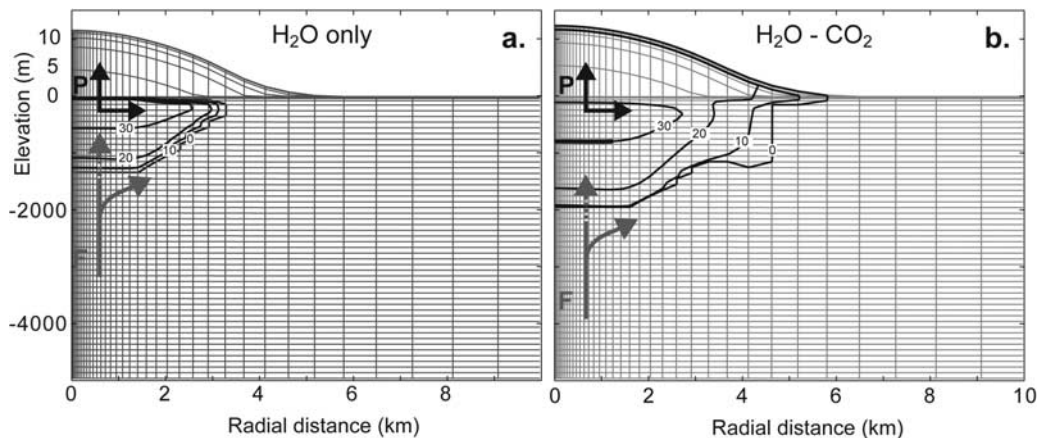

Figure 6. Cross section showing contours of gas saturation (%) for single-component (21 kt d^{-1} H_2O) and multicomponent (20 kt d^{-1} H_2O for 1 kt d^{-1} CO_2) simulations at a time of 20,000 years and permeability of 10^{-15} m^2 (Figure 4c). Pressure increases (P) associated with gas formation enhance the vertical and radial extent of deformation. Gas formation also reduces relative permeability (Figure 3), impeding vertical aqueous fluid flow (F) and deflecting warm fluids radially outward. (a) Single-component system showing radial and vertical extent of water vapor saturation. (b) Multicomponent system showing a much larger region occupied by the gas phase.
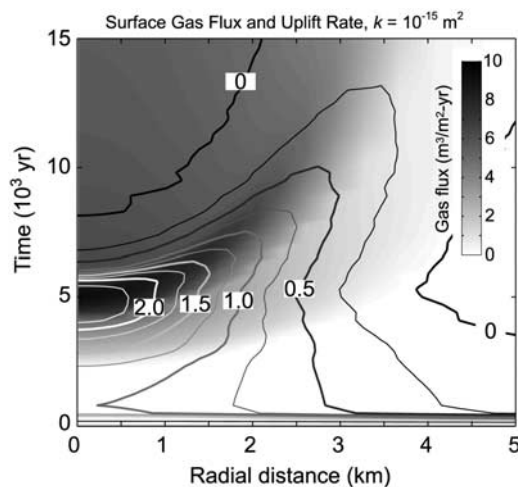
Figure 7. Temporal and spatial evolution of surface gas flux (m^3 m^{-2} a^{-1}; shaded) and uplift rate (mm a^{-1}; contours) when 20 kt d^{-1} of H_2O and 1 kt d^{-1} of CO_2 are injected into the base of a hydrothermal zone with a permeability of 10^{-15} m^2. After 2500 years of elapsed time gas discharge is evident at the surface at r = 0 (the center of the caldera). The highest local uplift rates are concurrent with the highest local gas flux. Both maxima migrate radially outward with time.

extend radially to a maximum distance of 3.1 km. In the multicomponent simulation, the entire subsurface to a depth of 2000 m and a radial distance of 5 km has gas saturations in excess of 10%.

[23] The vertical and radial extent of gas formation (Figure 6) and the related effects on GSD are both strongly influenced by permeability. When permeability and fluid injection rates are low (10^{-16} m^2 and 2.1 kt d^{-1}, respectively), calculated GSD from single-component and multicomponent simulations are virtually indistinguishable (Figure 5c). In contrast, when permeability and fluid injection rates are an order of magnitude higher (Figure 4c), vertical and radial extents of deformation are enhanced by 10% and 15%, respectively.

[24] When permeability is 10^{-15} m^2, there are brief periods when the magnitude and rate of uplift in the center of the caldera are lower in multicomponent simulations than in single-component ones (Figures 4a and 4b). Single-component simulations display a spike in central uplift rate coincident with rapid formation of steam in the shallow subsurface, whereas multicomponent simulations display a more gradual change coincident with development of a broad region of multiphase flow and associated reductions in relative permeability (Figures 3 and 6).

[25] The temporal and spatial evolution of fluid fluxes across the ground surface is largely controlled by the rate of fluid injection and permeability of the host rock. When permeability is 10^{-15} m^2, 2500 years elapse before surface gas discharge commences for the highest injection rate tested (Figure 7). Gas fluxes peak at ~9.5 m^3 m^{-2} a^{-1} in the center of the caldera after 5000 years of elapsed time, concurrent with the local maximum uplift rate of 2.4 mm a^{-1}. At later times, peak gas fluxes migrate radially outward, and are concurrent with local maximum uplift rates.

[26] A similar pattern is seen when permeability is an order of magnitude lower (Figure 8). Gas fluxes peak at 3 m^3 m^{-2} a^{-1} in the center of the caldera after 14,000 years have elapsed, concurrent with a local maximum uplift rate of 0.2 mm a^{-1}. Peak gas fluxes then migrate radially outward concurrent with local maximum uplift rates. In contrast to the higher-permeability simulation (Figure 7), local subsidence is apparent over a broad range of radial distances (1−8 km) and times (3−30 ka), as indicated by negative uplift rates.

5.2. Distributed Source Simulation

[27] We examine the effects of distributed source hydrothermal fluid injection and subsequent circulation on GSD for a permeability of 10^{-15} m^2. In this simulation, 10 kt d^{-1} of H_2O and 500 t d^{-1} of CO_2 are sourced uniformly over a radial distance of 9.5 km (Figure 2), corresponding to an injection area of ~300 km^2.

[28] Distributed fluid sourcing generates complex GSD patterns, including periods of localized uplift and subsidence, as shown in Figure 9. Compared to a point source simulation with the same injection rate and hydraulic parameters (Figures 4a and 4c), deformation begins with a much broader radial extent of displacement. Although the cumulative elevation gain in the center of the caldera (9.5 m) is roughly the same as for a point source, the maximum deformation is attained only after a much longer elapsed time (150,000 years versus 10,000 years). Cross sections showing GSD, thermal profiles, and fluid phase relations for times indicated in Figure 8 are shown in Figure 10.

[29] Distributed fluid injection along the base of the hydrothermal layer increases temperatures to >220°C (relative to an initial temperature of 180°C) at radial distances <9.5 km after 20,000 years of elapsed time (Figure 10a). Fluid injection and host rock thermal expansion generate a broad region of uplift extending 15 km from the center of
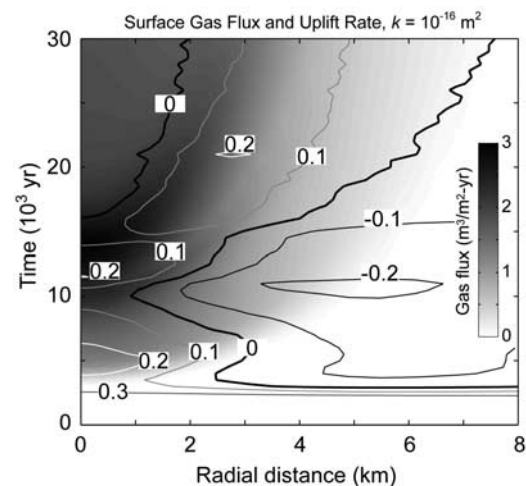

Figure 8. Temporal and spatial evolution of surface gas flux (m^3 m^{-2} a^{-1}; shaded) and uplift rate (mm a^{-1}; contours) when 20 kt d^{-1} of H_2O and 1 kt d^{-1} of CO_2 are injected into the base of a hydrothermal zone with a permeability of 10^{-16} m^2. The highest local uplift rates are concurrent with the highest local gas flux. Negative uplift rates correspond to regions experiencing subsidence.
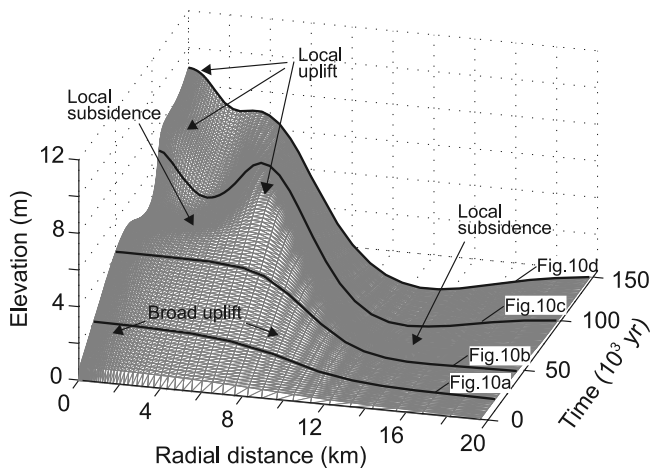
Figure 9. Temporal and spatial evolution of GSD for a simulation with permeability of 10^{-15} m^2 and fluids (10 kt d^{-1} H$_2$O, 500 t d^{-1} CO$_2$) injected over a radial distance of 9.5 km (an area of $\sim$300 km^2) along the base of the hydrothermal zone. The temporal and spatial evolution of GSD includes regions of broad uplift, localized uplift, and localized subsidence. Thick lines denote profiles shown in Figure 10, as labeled. Animation 7 shows system evolution.

the caldera. The difference in density at the base of the hydrothermal layer between hot (350°C) injected fluids and ambient (180°C) fluids distant from the injection area leads to pressure differences that drive lateral flow toward the caldera center and subsequent convection (Figure 10b). Elevated temperatures in the shallow subsurface lead to gas formation extending to depths of 500 m after 40,000 simulated years, and the radius of deformation contracts to 13.75 km at an average rate of 4 cm a^{-1} between 20,000 and 40,000 years of elapsed time.

[30] Continued fluid convection within permeable host rock generates separate convection cells after 90,000 years of elapsed time (Figure 10c), and deformation displays a multifaceted pattern of local uplift and subsidence. The regions of local uplift correspond to areas above the upwelling convection limbs, and local subsidence occurs above the adjoining downwelling limbs. Individual gas pockets with gas saturations in excess of 20% form within the locally uplifted regions, and gas concentrations are <1% within the locally subsiding region. The radial extent of deformation decreases to 10.5 km at an average rate of 8 cm a^{-1} between 40,000 and 90,000 years of elapsed time.

[31] After $\sim$150,000 simulation years the separate convection cells merge, and maximum uplift again becomes focused at the center of the caldera (Figure 10d). The radial extent of deformation decreases to 8.25 km at an average rate of 3.75 cm a^{-1} between 90,000 and 150,000 years. Temperatures at depths >100 m are in excess of 100°C, and a gas phase extends to depths of $\sim$1500 m, with saturations exceeding 25% in the upper 3–4 m over radial distances of 3 km, despite the cold (10°C) upper boundary condition.

6. Discussion and Conclusions

[32] Poroelastic models incorporating injection of magma-derived water and carbon dioxide into the overlying hydro-

thermal system generate substantial GSD in terms of rates (mm to cm a^{-1}), total magnitudes (up to tens of meters), and geometries (deformation occurring over radial distances of kilometers from the caldera center) on subannual to millennial timescales (Figures 4, 5, 9, and 10). Although our model results are nonunique in the sense that different combinations of parameters can generate similar deformation fields, results show deformation patterns induced by pore pressure transients at various timescales that are similar to those measured in several large calderas.

[33] At subannual to decadal timescales, the nature of deformation is largely controlled by poroelastic effects. The effect on GSD is most pronounced at the onset of fluid sourcing, with simulated uplift rates in the center of the caldera in excess of 10 cm a^{-1} for the highest sourcing rates tested (insets in Figures 4b and 5b). When fluids are broadly sourced over a radial distance of 9.5 km, volume increase leads to a broad pattern of uplift extending 15 km from the center of the caldera (Figures 9 and 10a).

[34] Over centennial to millennial timescales, host rock thermal expansion and deformation induced by hydrothermal fluid flow become more significant, and multiple fluid convection cells that can merge and split may generate complex GSD patterns including local regions of uplift and subsidence (Figures 9 and 10). Enhanced formation of a high-enthalpy gas phase in multicomponent (H$_2$O–CO$_2$) simulations (Figures 4–8) increases host rock inflation by up to 15% relative to single-component (liquid water) simulations when permeabilities are sufficiently high ($\geq$10^{-15} m^2). Gas fluxes across the ground surface at rates of m a^{-1} are evident only several thousand years after the onset of fluid injection, and the maximum local (in time) gas flux is concurrent with the maximum local uplift rate (Figures 7 and 8). In nature, more rapid gas migration may occur through high-permeability conduits and fractures, which are not represented in our simulations.

[35] At this stage our models do not try to explain any specific GSD episode but are exploratory in terms of determining which model parameters control the result. Without independent data, it is difficult to conclude whether specific episodes of observed caldera GSD result from magmatic intrusion or hydrothermal phenomena. We have shown that hydrothermal phenomena can potentially explain both short (months) and long (millennial) GSD episodes involving large spatial scales, temporal variability, and changing sign (uplift or subsidence). It seems reasonable to surmise that some specific GSD episodes involving strong spatial and temporal variability and changing sign may indeed have hydrothermal origins. Explaining such episodes in terms of changes in magma volume in an elastic medium can require complex composite magma intrusion models involving multiple discrete sources.

[36] Several lines of indirect evidence suggest that subsurface volume changes and caldera deformation may sometimes be associated with the dynamics of a low-viscosity, low-density, CO$_2$-rich fluid at shallow depths. For example, recent episodes of inflation and deflation in the Campi Flegrei caldera correlate with CO$_2$/H$_2$O transients measured at the ground surface, suggesting that CO$_2$ pressures are high during inflation events [*Chiodini et al.*, 2003]. The large volume of diffuse CO$_2$ (45 ± 16 kt d^{-1}) discharge from the Yellowstone volcanic system [*Werner*
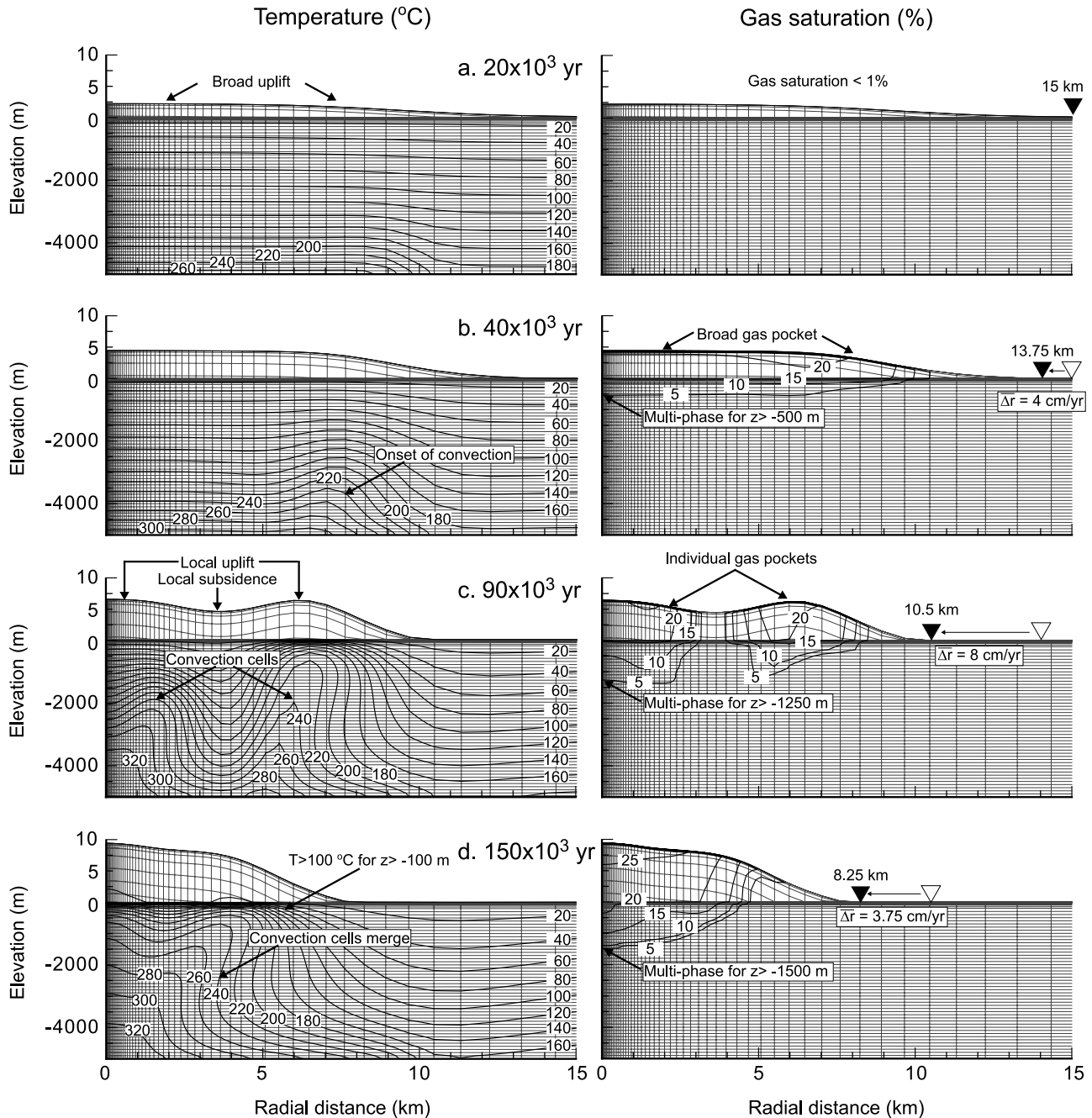
Figure 10. Cross sections showing contours of temperature and gas saturation for profiles shown in Figure 9. For purposes of illustration, vertical deformation above initial ground surface elevation (z = 0) has been exaggerated 200-fold. Solid inverted triangles denote maximum radial extent of deformation. Open inverted triangles denote maximum extent from previous panel, and the difference is used to calculate the average rate of contraction of the deformed zone, as labeled. (a) After 20 ka. (b) After 40 ka. (c) After 90 ka. (d) After 150 ka.

and Brantley, 2003] cannot be sustained by discrete episodes of magma intrusion into the upper crust during periods of inflation [*Lowenstern and Hurwitz*, 2008], suggesting that some of the observed deformation may be associated with the dynamics of the hydrothermal system. In fact, the involvement of gas-rich fluids in recent deformation of the Yellowstone caldera may be inferred from abrupt changes in uplift concurrent with elevated seismicity [*Waite and Smith*, 2002].

[37] Recent advances in geodetic measurement techniques continue to provide better spatial and temporal resolution of GSD in hydrothermally active calderas. Methods for monitoring and quantifying volcanic gas discharge also continue to improve. Continuous, high-precision microgravity measurements may discriminate between basalt intrusion and aqueous fluid injection at shallow depths, due to the threefold (or more) difference in density between magma and H_2O-CO_2 fluid [e.g., *Battaglia and Segall*, 2004;

Battaglia et al., 2006; *de Zeeuw-van Dalfsen et al.*, 2005; *Gottsmann and Rymer*, 2002; *Rymer*, 1994]. When combined with quantitative dynamic models [*Todesco and Berrino*, 2005], such data sets may provide insights into the nature of the fluid(s) inducing deformation. Monitoring of deep pore fluid processes could also be diagnostic but requires access to deep boreholes, which are often unavailable.

[38] This study focused on simulations of poroelastic deformation induced by multicomponent (H_2O-CO_2) and multiphase (liquid-gas) fluid flow. Using a range of hydrologically plausible model parameters and fluid-sourcing configurations, results display a range of GSD rates, magnitudes, and geometries similar to those seen in several large calderas. Despite simplifications such as homogeneous, isotropic rock property distributions and constant rate fluid sourcing, multifaceted deformation patterns (including periods of localized uplift and subsidence) emerged. Heterogeneous property distributions (including high-permeability cracks) will affect both the extent and magnitude of deformation and rates and patterns of fluid flow, and are currently being tested using more sophisticated models. The potential for both rapid and gradual GSD resulting from magma-derived aqueous fluids, as demonstrated in this study, suggests that hydrothermal fluid circulation may help explain some occurrences of GSD that have not culminated in magmatic eruptions.

References

Anderson, A. T., Jr., S. Newman, S. N. Williams, T. H. Druitt, C. Skirius, and E. Stolper (1989), H_2O, CO_2, Cl, and gas in Plinian and ash-flow Bishop rhyolite, *Geology*, *17*, 221–225.

Battaglia, M., and P. Segall (2004), The interpretation of gravity changes and crustal deformation in active volcanic areas, *Pure Appl. Geophys.*, *161*, 1453–1467, doi:10.1007/s00024-004-2514-5.

Battaglia, M., C. Troise, F. Obrizzo, F. Pingue, and G. De Natale (2006), Evidence for fluid migration as the source of deformation at Campi Flegrei caldera (Italy), *Geophys. Res. Lett.*, *33*, L01307, doi:10.1029/2005GL024904.

Bauer, S. J., and J. Handin (1983), Thermal-expansion and cracking of 3 confined, water-saturated igneous rocks to 800°C, *Rock Mech. Rock Eng.*, *16*, 181–198.

Bibby, H. M., T. G. Caldwell, F. J. Davey, and T. H. Webb (1995), Geophysical evidence on the structure of the Taupo Volcanic Zone and its hydrothermal circulation, *J. Volcanol. Geotherm. Res.*, *68*, 29–58.

Bjornsson, G., and G. Bodvarsson (1990), A survey of geothermal reservoir properties, *Geothermics*, *19*, 17–27, doi:10.1016/0375-6505(90)90063-H.

Chang, W. L., R. B. Smith, C. Wicks, J. M. Farrell, and C. M. Puskas (2007), Accelerated uplift and magmatic intrusion of the Yellowstone Caldera, 2004 to 2006, *Science*, *318*, 952–956, doi:10.1126/science.1146842.

Chiodini, G., F. Frondini, C. Cardellini, D. Granieri, L. Marini, and G. Ventura (2001), CO_2 degassing and energy release at Solfatara volcano, Campi Flegrei, Italy, *J. Geophys. Res.*, *106*, 16,213–16,221, doi:10.1029/2001JB000246.

Chiodini, G., M. Todesco, S. Caliro, C. Del Gaudio, G. Macedonio, and M. Russo (2003), Magma degassing as a trigger of bradyseismic events: The case of Phlegrean Fields (Italy), *Geophys. Res. Lett.*, *30*(8), 1434, doi:10.1029/2002GL016790.

Corey, A. T. (1957), Measurement of water and air permeabilities in unsaturated soil, *Soil Sci. Soc. Am. J.*, *21*, 7–10.

Davis, P. M. (1986), Surface deformation due to inflation of an arbitrarily oriented triaxial ellipsoidal cavity in an elastic half-space, with reference to Kilauea Volcano, Hawaii, *J. Geophys. Res.*, *91*, 7429–7438, doi:10.1029/JB091iB07p07429.

de Zeeuw-van Dalfsen, E., H. Rymer, F. Sigmundsson, and E. Sturkell (2005), Net gravity decrease at Askja volcano, Iceland: Constraints on processes responsible for continuous caldera deflation, 1988–2003, *J. Volcanol. Geotherm. Res.*, *139*, 227–239, doi:10.1016/j.jvolgeores.2004.08.008.

Duan, Z., and Z. Zhang (2006), Equation of state of the H_2O, CO_2, and H_2O-CO_2 systems up to 10 GPa and 2573.15 K: Molecular dynamics simulations with ab initio potential surface, *Geochim. Cosmochim. Acta*, *70*, 2311–2324, doi:10.1016/j.gca.2006.02.009.

Dvorak, J. J., and D. Dzurisin (1997), Volcano geodesy: The search for magma reservoirs and the formation of eruptive vents, *Rev. Geophys.*, *35*, 343–384, doi:10.1029/97RG00070.

Dzurisin, D. (2003), A comprehensive approach to monitoring volcano deformation as a window on the eruption cycle, *Rev. Geophys.*, *41*(1), 1001, doi:10.1029/2001RG000107.

Dzurisin, D. (2007), *Volcano Deformation*, 476 pp., Springer Praxis, London.

Dzurisin, D., J. C. Savage, and R. O. Fournier (1990), Recent crustal subsidence at Yellowstone Caldera, Wyoming, *Bull. Volcanol.*, *52*, 247–270, doi:10.1007/BF00304098.

Fialko, Y., Y. Khazan, and M. Simons (2001), Deformation due to a pressurized horizontal circular crack in an elastic half-space, with applications to volcano geodesy, *Geophys. J. Int.*, *146*, 181–190, doi:10.1046/j.1365-246X.2001.00452.x.

Fournier, R. O. (1999), Hydrothermal processes related to movement of fluid from plastic into brittle rock in the magmatic-epithermal environment, *Econ. Geol.*, *94*, 1193–1211, doi:10.2113/gsecongeo.94.8.1193.

Gerlach, T. M., M. P. Doukas, K. A. McGee, and R. Kessler (1999), Airborne detection of diffuse carbon dioxide emissions at Mammoth Mountain, California, *Geophys. Res. Lett.*, *26*, 3661–3664, doi:10.1029/1999GL008388.

Giggenbach, W. F. (1984), Mass transfer in hydrothermal alteration systems-A conceptual approach, *Geochim. Cosmochim. Acta*, *48*, 2693–2711, doi:10.1016/0016-7037(84)90317-X.

Giggenbach, W. F. (1988), Geothermal solute equilibria: Derivation of Na-K-Mg-Ca geoindicators, *Geochim. Cosmochim. Acta*, *52*, 2749–2765.

Goff, F., and C. J. Janik (2002), Gas geochemistry of the Valles caldera region, New Mexico and comparisons with gases at Yellowstone, Long Valley and other geothermal systems, *J. Volcanol. Geotherm. Res.*, *116*, 299–323, doi:10.1016/S0377-0273(02)00222-6.

Gottsmann, J., and H. Rymer (2002), Deflation during caldera unrest: Constraints on subsurface processes and hazard prediction from gravity-height data, *Bull. Volcanol.*, *64*, 338–348, doi:10.1007/s00445-002-0212-7.

Gottsmann, J., R. Carniel, N. Coppo, L. Wooller, S. Hautmann, and H. Rymer (2007), Oscillations in hydrothermal systems as a source of periodic unrest at caldera volcanoes: Multiparameter insights from Nisyros, Greece, *Geophys. Res. Lett.*, *34*, L07307, doi:10.1029/2007GL029594.

Heard, H. C., and L. Page (1982), Elastic moduli, thermal expansion, and inferred permeability of two granites to 350°C and 55 megapascals, *J. Geophys. Res.*, *87*, 9340–9348.

Hill, D. P. (1992), Temperatures at the base of the seismogenic crust beneath Long Valley Caldera, California, and the Phlegrean Fields caldera, Italy, in *Volcanic Seismology*, edited by P. Gasparini et al., pp. 432–461, Springer, New York.

Horne, R. N., and H. J. Ramey (1978), Steam/water relative permeabilities from production data, *Trans. Geotherm. Resour. Counc.*, *2*, 291–293.

Hsieh, P. A. (1996), Deformation-induced changes in hydraulic head during ground-water withdrawal, *Ground Water*, *34*, 1082–1089.

Hurwitz, S., K. L. Kipp, S. E. Ingebritsen, and M. E. Reid (2003), Groundwater flow, heat transport, and water table position within volcanic edifices: Implications for volcanic processes in the Cascade Range, *J. Geophys. Res.*, *108*(B12), 2557, doi:10.1029/2003JB002565.

Hurwitz, S., L. B. Christiansen, and P. A. Hsieh (2007), Hydrothermal fluid flow and deformation in large calderas: Inferences from numerical simulations, *J. Geophys. Res.*, *112*, B02206, doi:10.1029/2006JB004689.

Kaszuba, J. P., L. L. Williams, D. R. Janecky, W. K. Hollis, and I. N. Tsimpanogiannis (2006), Immiscible CO_2-H_2O fluids in the shallow crust, *Geochem. Geophys. Geosyst.*, *7*, Q10003, doi:10.1029/2005GC001107.

Kwoun, O. I., Z. Lu, C. Neal, and C. Wicks Jr. (2006), Quiescent deformation of the Aniakchak Caldera, Alaska mapped by InSAR, *Geology*, *34*, 5–8, doi:10.1130/G22015.1.

Lachenbruch, A. H., J. H. Sass, R. J. Munroe, and T. H. Moses Jr. (1976), Geothermal setting and simple heat conduction models for the Long Valley Caldera, *J. Geophys. Res.*, *81*, 769–784.

Li, K., and R. N. Horne (2007), Systematic study of steam-water capillary pressure, *Geothermics*, *36*, 558–574, doi:10.1016/j.geothermics.2007.08.002.

Lowenstern, J. B. (2001), Carbon dioxide in magmas and implications for hydrothermal systems, *Miner. Deposita*, *36*, 490–502, doi:10.1007/s001260100185.

Lowenstern, J. B., and S. Hurwitz (2008), Monitoring a supervolcano in repose: Heat and volatile flux at the Yellowstone caldera, *Elements*, *4*, 35–40, doi:10.2113/GSELEMENTS.4.1.35.

Manconi, A., T. R. Walter, and F. Amelung (2007), Effects of mechanical layering on volcano deformation, *Geophys. J. Int.*, *170*, 952–958, doi:10.1111/j.1365-246X.2007.03449.x.

Manning, C. E., and S. Ingebritsen (1999), Permeability of the continental crust: The implications of geothermal data and metamorphism systems, *Rev. Geophys.*, *37*, 127–150, doi:10.1029/1998RG900002.

Masterlark, T. (2007), Magma intrusion and deformation predictions: Sensitivities to the Mogi assumptions, *J. Geophys. Res.*, *112*, B06419, doi:10.1029/2006JB004860.

Mogi, K. (1958), Relations of the eruptions of various volcanoes and the deformation of ground surfaces around them, *Bull. Earthquake Res. Inst. Univ. Tokyo*, *36*, 94–134.

Newman, S., S. Epstein, and E. Stolper (1988), Water, carbon dioxide, and hydrogen isotopes in glasses from the ca. 1340 A.D. eruption of the Mono Craters, California: Constraints on degassing phenomena and initial volatile content, *J. Volcanol. Geotherm. Res.*, *35*, 75–96.

Piquemal, J. (1994), Saturated steam relative permeabilities of unconsolidated porous media, *Transp. Porous Media*, *17*, 105–120.

Poland, M., M. Hamburger, and A. Newman (2006), The changing shapes of active volcanoes: History, evolution, and future challenges for volcano geodesy, *J. Volcanol. Geotherm. Res.*, *150*, 1–13, doi:10.1016/j.jvolgeores.2005.11.005.

Pritchard, M. E., and M. Simons (2002), A satellite geodetic survey of large-scale deformation of volcanic centres in the central Andes, *Nature*, *418*, 167–171, doi:10.1038/nature00872.

Pruess, K. (2005), The TOUGH codes-A family of simulation tools for multiphase flow and transport processes in permeable media, *Vadose Zone J.*, *3*, 738–746.

Rymer, H. (1994), Microgravity change as a precursor to volcanic activity, *J. Volcanol. Geotherm. Res.*, *61*, 311–328, doi:10.1016/0377-0273(94)90011-6.

Seward, T. M., and D. M. Kerrick (1996), Hydrothermal CO_2 emission from the Taupo Volcanic Zone, New Zealand, *Earth Planet. Sci. Lett.*, *139*, 105–113, doi:10.1016/0012-821X(96)00011-8.

Sherburn, S., S. Bannister, and H. Bibby (2003), Seismic velocity structure of the central Taupo Volcanic Zone, New Zealand, from local earthquake tomography, *J. Volcanol. Geotherm. Res.*, *122*, 69–88, doi:10.1016/S0377-0273(02)00470-5.

Sorey, M. L., M. A. Grant, and E. Bradford (1980), Nonlinear effects in two-phase flow to wells in geothermal reservoirs, *Water Resour. Res.*, *16*, 767–777.

Spycher, N., K. Pruess, and J. Ennis-King (2003), CO_2-H_2O mixtures in the geological sequestration of CO_2. I. Assessment and calculation of mutual solubilities from 12 to 100°C and up to 600 bar, *Geochim. Cosmochim. Acta*, *67*, 3015–3031, doi:10.1016/S0016-7037(03)00273-4.

Todesco, M., and G. Berrino (2005), Modeling hydrothermal fluid circulation and gravity signals at the Phlegraean Fields caldera, *Earth Planet. Sci. Lett.*, *240*, 328–338, doi:10.1016/j.epsl.2005.09.016.

Todesco, M., J. Rutqvist, G. Chiodini, K. Pruess, and C. M. Oldenburg (2004), Modeling of recent volcanic episodes at Phlegrean Fields (Italy): Geochemical variations and ground deformation, *Geothermics*, *33*, 531–547, doi:10.1016/j.geothermics.2003.08.014.

Turcotte, D. L., and G. Schubert (2002), *Geodynamics*, 2nd ed., 472 pp., Cambridge Univ. Press, New York.

Waite, G. P., and R. B. Smith (2002), Seismic evidence for fluid migration accompanying subsidence of the Yellowstone caldera, *J. Geophys. Res.*, *107*(B9), 2177, doi:10.1029/2001JB000586.

Watson, I. M., et al. (2000), The relationship between degassing and ground deformation at Soufriere Hills Volcano, Montserrat, *J. Volcanol. Geotherm. Res.*, *98*, 117–126, doi:10.1016/S0377-0273(99)00187-0.

Werner, C., and S. Brantley (2003), CO_2 emissions from the Yellowstone volcanic system, *Geochem. Geophys. Geosyst.*, *4*(7), 1061, doi:10.1029/2002GC000473.

Wicks, C. W., W. Thatcher, D. Dzurisin, and J. Svarc (2006), Uplift, thermal unrest and magma intrusion at Yellowstone Caldera, *Nature*, *440*, 72–75, doi:10.1038/nature04507.

Wohletz, K., L. Civetta, and G. Orsi (1999), Thermal evolution of the Phlegraean magmatic system, *J. Volcanol. Geotherm. Res.*, *91*, 381–414, doi:10.1016/S0377-0273(99)00048-7.

Wong, T. F., and W. F. Brace (1979), Thermal expansion of rocks: Some measurements at high pressure, *Tectonophysics*, *57*, 95–117, doi:10.1016/0040-1951(79)90143-4.

———————————

P. A. Hsieh, S. Hurwitz, M. Hutnak, and S. E. Ingebritsen, U.S. Geological Survey, 345 Middlefield Road, MS 434, Menlo Park, CA 94025, USA. (mhutnak@usgs.gov)